



POLITECNICO
MILANO 1863

RE.PUBLIC@POLIMI

Research Publications at Politecnico di Milano

Post-Print

This is the accepted version of:

M.C. Morelli, T. Bellosta, A. Donizetti, A. Guardone
Assessment of the PoliMIce toolkit from the 1st AIAA Ice Prediction Workshop
in: AIAA Aviation 2022 Forum, AIAA, 2022, ISBN: 9781624106354, p. 1-21, AIAA 2022-3307
[AIAA Aviation 2022 Forum, Chicago, IL, USA & Virtual, 27 June-1 July 2022]
doi:10.2514/6.2022-3307

The final publication is available at <https://doi.org/10.2514/6.2022-3307>

Access to the published version may require subscription.

When citing this work, cite the original published paper.

Permanent link to this version

<http://hdl.handle.net/11311/1220295>

Assessment of the PoliMIce toolkit from the 1st AIAA Ice Prediction Workshop

Myles Morelli * Tommaso Bellosta † Alessandro Donizetti ‡ and Alberto Guardone §
*Department of Aerospace Science and Technology, Politecnico di Milano
Building B12, Via La Masa 34, Milano, MI 20156, Italy*

This paper presents the Politecnico di Milano Icing Research Group’s contribution to the 1st AIAA Ice Prediction Workshop. A collection of two- and three-dimensional test cases to predict the collection efficiency and ice accretion are simulated using the PoliMIce ice accretion software suite. Test cases include the prediction of the collection efficiency on a three-element-airfoil and on a full-scale horizontal swept tail plane. Additionally, test cases for the simulation of ice shapes on a NACA23012 airfoil and on swept wings with varying degrees of sweep angle are assessed. The numerical predictions are evaluated and compared to high quality experimental measurements taken from the NASA Glenn Icing Research Tunnel. In general the numerical predictions compare favourably with the experimental measurements. Key droplet impingement characteristics including the collection efficiency peak and impingement limits are captured. Meanwhile distinctive ice features of rime and glaze ice regimes are depicted in the simulations. However, there remains scope for further improvement of models as highlighted by the more challenging test cases such as the three-element-airfoil and the test cases which produce glaze ice shapes with large horns.

I. Introduction

In-flight icing encounters can adversely affect the performance characteristics and handling qualities of aircraft [1]. The rapid build up of ice on the leading edge of aerodynamic lifting surfaces such as wings can significantly disrupt the flow behaviour. Ice structures may potentially even cause flow separation leading to ice induced stall at unexpectedly low angles-of-attack. Consequently, aircraft icing has become an increasingly important safety critical issue. This is highlighted by the recent investment in major international networks such as ICE-GENESIS which seeks to provide the European aeronautical industry with a new generation of validated numerical simulation tools and icing wind tunnels for the safe, efficient and cost effective design and certification of future aircraft [2]. Networks such as ICE-GENESIS have been established as numerical ice predictions are only as credible as the models are reliable. The validation and verification of numerical models is therefore pertinent if the end goal is to use simulation tools for the design and certification of aircraft. Establishing best practices for ice prediction is key if simulation tools are to continue to progress.

In conjunction with the AIAA AVIATION 2021 Forum, the 1st Ice Prediction Workshop was founded with the objective of: (1) ice shape comparisons between two- and three-dimensional codes where experimental ice shapes are readily available; and (2) establishing a sound baseline of current simulation capabilities which can subsequently be used for future Ice Prediction Workshops [3]. The 1st Ice Prediction Workshop aimed to bring together industry and academia to provide a collaborative platform for cross-code model comparison and verification. Furthermore, the Ice Prediction Workshop organizing committee established an open data base of experimental test cases which could be used for model validation. The workshop included test cases for predicting the collection efficiency and ice accretion on two- and three-dimensional geometries. The test cases were selected to challenge existing numerical models and to identify the current limitations of simulation tools.

A conventional fixed-wing icing simulation structure routinely involves a three-stage process which iteratively updates to account for unsteady ice accretion. This simulation process is commonly known as multi-step ice accretion and is adopted by PoliMIce in this work. A schematic of multi-step ice accretion is shown in Fig. 1. The first stage involves the use of a flow solver to determine the aerodynamic flow-field around regions exposed to icing such as the wing,

*Post Doctoral Researcher, mylescarlo.morelli@polimi.it

†Ph.D. Candidate, tommaso.bellosta@polimi.it

‡Ph.D. Candidate, alessandro.donizetti@mail.polimi.it

§Full Professor, alberto.guardone@polimi.it

fuselage or even pitot tube. The second stage entails the use of a droplet solver to compute the trajectories of supercooled water droplets in the fluid flow to determine their impingement locations and collection efficiency. The third stage concerns the use of an icing solver to calculate the ice shape based on icing models which are dependent on the surface temperature and collection efficiency as well as other influential parameters. Multi-step ice accretion then introduces a fourth stage to update the iced mesh usually through means of mesh deformation techniques. Two-dimensional multi-step ice accretion simulations are now relatively commonplace [4–6]. However, robust three-dimensional multi-step ice accretion simulations extend beyond the current state-of-the-art. Establishing the best practises for three-dimensional multi-step ice accretion is a long-term goal and was one of the main objectives of the 1st Ice Prediction Workshop.

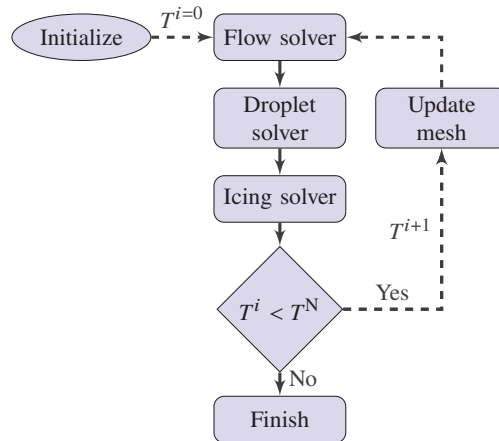


Fig. 1 Schematic of a standard multi-step icing simulation.

In this work the Politecnico di Milano Icing Research Group’s contribution to the 1st AIAA Ice Prediction Workshop is presented. The contribution from Politecnico di Milano utilizes the PoliMIce ice accretion simulation software for the prediction of ice shapes. PoliMIce was initially developed by Gori et al. [6] for the simulation of two- and three-dimensional aircraft ice shapes. The PoliMIce ice accretion software includes state-of-the-art ice formation models including the local exact solution of the unsteady Stefan problem [7]. Furthermore, PoliMIce has a unique set of prediction capabilities which sets it apart from other ice accretion solvers. PoliMIce has uniquely been developed for predicting rotorcraft ice accretion and shedding [8, 9]. It has also been utilized for the innovative design of rotorcraft acoustic ice detection technologies [10, 11]. PoliMIce has also been extensively developed for the simulation and robust design optimization of thermal ice protection systems (IPS) [12, 13]. Additionally it has been utilized for the optimization of heat fluxes in uncertain cloud environments [14]. To that end, PoliMIce has also be utilized to investigate Uncertainty Quantification (UQ) in icing conditions [15]. The aim of this work is to further validate the PoliMIce ice accretion software using the test cases from the 1st AIAA Ice Prediction Workshop.

The organization of the paper is as follows: the 1st AIAA Ice Prediction Workshop is discussed in detail in Section II; the PoliMIce ice accretion software is introduced in Section III; the Ice Prediction Workshop test cases and numerical predictions are discussed in Section IV; the concluding remarks from this work are highlighted in Section V.

II. Ice Prediction Workshop

The 1st Ice Prediction Workshop was held virtually in conjunction with the AIAA AVIATION 2021 Forum from 26-29 July 2021. It was the first workshop of its kind, bringing together academia and industry to understand the current ice prediction simulation capabilities and limitations. The organizing committee of the 1st Ice Prediction Workshop identified a series open experimental data bases which could subsequently be utilized by participants for code validation. The experimental data included information on the collection efficiency and ice shapes on challenging geometries of interest. During the 1st Ice Prediction Workshop the organizing committee and volunteers gathered and compared the simulation results from each of the participants. The outcome was the first icing code-to-code comparison to assess and verify different icing models. This in itself was a significant achievement to aid in the progression of best practises for icing codes. The Politecnico di Milano Icing Research Group contributed to the 1st AIAA Ice Prediction Workshop as a participant. The test cases simulated by the Politecnico di Milano Icing Research Group are highlighted in Table 1. In

total, all of the mandatory test cases from the workshop were covered. In addition, several of the optional test cases which focused on Appendix O conditions were also simulated.

Table 1 Test cases simulated by Politecnico di Milano.

Test Case	Category	Configuration	Key Information
Case-111	3D Droplet impingement	NACA64A008 horizontal tail	MVD 21
Case-112	3D Droplet impingement	NACA64A008 horizontal tail	MVD 92
Case-121	2D Droplet impingement	Three-element-airfoil	MVD 21
Case-122	2D Droplet impingement	Three-element-airfoil	MVD 92
Case-241	2D Ice accretion	18-inch NACA23012	Rime
Case-242	2D Ice accretion	18-inch NACA23012	Glaze
Case-361	3D Ice accretion	NACA0012 30° sweep	Rime
Case-362	3D Ice accretion	NACA0012 30° sweep	Glaze
Case-371	3D Ice accretion	NACA0012 45° sweep	Rime
Case-372	3D Ice accretion	NACA0012 45° sweep	Glaze

III. PoliMice Framework

A. Aerodynamic Analysis

The SU2 software suite [16] is an open-source toolkit written in C++ and Python created for multi-physics simulation and design. It is built specifically for the analysis of partial differential equations (PDEs) and PDE-constrained optimization problems on unstructured meshes with state-of-the-art methods and algorithms, and is particularly well suited for aerodynamic shape design. A node centered Finite volume method (FVM) is applied on arbitrary unstructured meshes using a standard edge-based data structure on a dual grid with median-dual control volumes. Convective fluxes are discretized at each edge mid point using either centered or upwind schemes. Discretization using upwind schemes can be coupled with a linear reconstruction via the MUSCL approach to yield a second order scheme in space. Viscous fluxes are discretized using a corrected average of gradients approach. Source terms are approximated at each node using a piecewise constant reconstruction within each control volume. Gradients are obtained via a weighted least-squares approach. Regarding time integration, SU2 is capable to solve implicitly steady and unsteady problems, using a dual-time stepping strategy, leading to second-order accuracy and time. The core of the suite is a Reynolds-averaged Navier-Stokes (RANS) solver which is used in this study in tandem with the Spalart–Allmaras (SA) turbulence model. The application towards its use for the simulation of rotorcraft flows has recently been highlighted by Ref.[17].

B. Particle Tracking

Simulating the ice accretion phenomenon formally involves the computation of the two phase flow of water and air. This can be done for instance with the Euler-Euler approach using a two-fluid formulation [18]. Due to the scales at play in ice accretion such flows are only one-way coupled and the computation of the aerodynamics can be performed independently of the water droplets. An in-house particle tracking code based on a Lagrangian framework was developed at Politecnico di Milano and is used for the simulation of clouds containing supercooled water droplets [19]. The aim of the droplet solver is that of computing the collection efficiency β over the aircraft, which is used to compute the water mass that is collected at a given location on the surface. The Lagrangian framework allows a straightforward modelling of supercooled water droplets effects, such as splashing effects, aerodynamic breakup, deformation and can deal with secondary particles.

The cloud impinging the aircraft surfaces, is represented as a single front initially placed at an arbitrary distance ahead of the aircraft. This distance is set so that droplets are traced starting from an unperturbed region of the domain and so that the computational burden related to the trajectory time integration, proportional to the integration length, is bearable. In three-dimensional problems, this front consists of a two-dimensional layer of droplets uniformly distributed. In a two-dimensional setting the layer degenerates into a straight line. As the final result depends on the particle

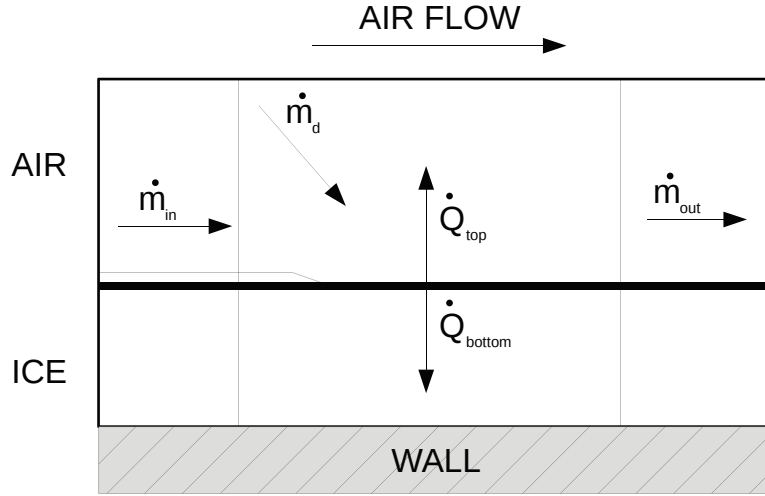


Fig. 2 Simplified scheme of the one dimensional phase change problem solved in each computational cell to obtain the thickness of growing ice.

resolution, a strategy was developed to automatically refine the seeding region by adding new particles where needed. The seeding front, initially uniform, is discretized as a structured mesh of linear (in 2D) or quadrilateral (in 3D) elements. Elements are incrementally split at each iteration which consists of evolving the current cloud front and computing β on the surface. The simulation stops when the difference in $L2$ norm between two consecutive collection efficiency calculations is below a user supplied threshold. In practical applications, clouds are poly-dispersed. A standard approach deals with this problem by tracking a uniform cloud of droplets with diameter equal to the Median Volume Diameter (MVD). That is the particle size that divides the total mass of the cloud in two. Half the mass is coming from droplets of diameter smaller than the cloud MVD, half from particles larger than the MVD. A more refined discretization of the particle size distribution can be taken into account by subdividing the droplets size probability distribution function in a given number of bins. For each bin, a simulation can be performed and the final collection efficiency can be obtained as a weighted sum of the bins' β .

Techniques to allow for particle tracking in mesh with arbitrary motion and across non-conformal boundary interfaces are used within this work to simulate clouds entrained within rotorcraft flow-fields [20].

C. Ice Accretion

The in-house code PoliMIce is used for computing the ice accretion [6]. Computing the thickness of the accreting ice layer amounts to solving a phase change problem over the aircraft surface. Typically surfaces are first discretized in computational cells, and a one-dimensional Stefan problem ([21]) is solved for each control volume. Cells are coupled via boundary conditions enforcing the conservation of mass at cell interfaces, through specific terms representing the amount of unfrozen water entering or leaving the cell (\dot{m}_{in} , \dot{m}_{out}) under the action of the external flow or inertial forces. The elemental problem solved for in each computational cell is represented in Figure 2. The position of the air-ice or water-ice interface is computed by solving a heat balance involving the quantities shown in the figure. The mass rates \dot{m}_{in} , \dot{m}_{out} and \dot{m}_d account for the liquid water mass coming, respectively, from the upwind and downwind control cells and from the droplets. The terms \dot{Q}_{top} and \dot{Q}_{bottom} are the thermal power contributions. \dot{Q}_{top} includes heat exchange with the air flow via convection or friction and accounts for the power due to the droplets kinetic energy. \dot{Q}_{bottom} accounts for the thermal power dissipated via conduction thorough the ice layer to the aircraft structure.

To solve the above problem, PoliMIce implements a local exact solution of the unsteady Stefan problem [22]. It employs an extension of the Myers model explicitly accounting for the mass fluxes related to sublimation and a more detailed description of the liquid film flow above the ice surface. In glaze conditions, the unsteady description of the heat diffusion problem in the ice layer is based on the exact local solution of the unsteady Stefan problem. The term

\dot{Q}_{bottom} is therefore computed as:

$$\begin{aligned}\dot{Q}_{\text{bottom}} &= k_i \frac{T_{\text{freezing}} - T_{\text{wall}}}{\text{erf}(\lambda)} \frac{e^{-\lambda^2} \sqrt{\rho_i C_P}}{\sqrt{\pi k_i t}} \\ \lambda(t) &= \frac{B(t) \sqrt{\rho_i C_P}}{\sqrt{k_i}}\end{aligned}\quad (1)$$

where k_i and ρ_i are the thermal conductivity and density of ice, and B is the ice layer thickness. To close the energy balance on each cell, the \dot{Q}_{top} power is computed by considering convection, evaporation, latent heat, friction and kinetic heat transfers. All terms are modeled according to specific closures reported in [6].

Eventually, the accretion rate can be obtained as:

$$\begin{aligned}\frac{\partial B}{\partial t} &= \frac{\dot{m}_d + \dot{m}_{in} - \dot{m}_{out}}{A \rho_i}, \quad \text{if } B < B_g \\ \frac{\partial B}{\partial t} &= \frac{1}{\rho_i L_f} (\dot{Q}_{\text{top}} + \dot{Q}_{\text{bottom}}), \quad \text{if } B \geq B_g\end{aligned}\quad (2)$$

where A is the area of the computational cell and L_f is the ice latent heat of fusion. B_g is the rime limit thickness and is computed as:

$$B_g = \frac{1}{2} \frac{A k_i (T_{\text{freezing}} - T_{\text{wall}})}{L_f (\dot{m}_d - \dot{Q}_s L_s^{-1}) - \dot{Q}_{\text{top}}}\quad (3)$$

The ice shapes are then computed using a multi-step approach, whereby non-linear ice accretion is accounted for by iteratively updating the surface solution on which the ice accretes.

D. Mesh Deformation

Radial Basis Function (RBF) mesh deformation techniques are used to update the iced mesh. RBF mesh deformation techniques are robust and preserve high-quality mesh even during large deformations. Furthermore, the potential of RBF mesh deformation techniques for non-smooth, local deformations such as those present during aircraft icing has been demonstrated by Ref.[23]. However, it is computational prohibitive to use standard RBF mesh deformation on large data sets. To address this concern, multi-level greedy surface point selection algorithms [24] and volume point reduction methods [25] are introduced to improve the computational expense of RBF mesh deformation.

IV. Test Cases

A. Case-111, 112

The first test cases presented are Case-111 and Case-112. The focus of the test cases is to assess the three-dimensional prediction of the collection efficiency. The extensive experimental database from Papadakis et al. [26] is used for the validation of water droplet impingement models on three-dimensional geometries. The experimental tests were conducted in the NASA Glenn Icing Research Tunnel (IRT) on a range of configurations. The experimental tests included measurements of the flow and water droplet impingement. The configuration of Case-111 and Case-112 is the outboard portion of a full-scale horizontal swept tail from a general business jet with a NACA 64A008 profile. The operating conditions are shown in Table 2. The operating conditions of Case-111 are representative of Appendix C, meanwhile the operating conditions from Case-112 are representative of Appendix O conditions.

Table 2 Horizontal Tail Test Conditions Ref. [26].

Mach	AoA	Pressure	Temp	MVD	Re	Chord
[-]	[°]	[Pa]	[K]	[g m ⁻³]	[-]	[in]
0.23	6.0	83,025	291.2	21, 92	5.03×10 ⁶	37.65

The mesh provided by the 1st Ice Prediction Workshop is used for simulating Case-111 and Case-112. The mesh contains approximately 16 750 000 volume elements meanwhile approximately 120 000 surface elements are used for

the discretization of the wing geometry. The mesh contains a structured boundary layer which satisfies $y^+ < 1$ to fully resolve viscous effects within the boundary layer. The external NASA IRT walls are incorporated in the mesh. Inlet and outlet boundary conditions are subsequently applied to the appropriate wind tunnel boundaries.

The numerical methods for computing the flow field in SU2 are now discussed. Roe's second-order upwind scheme is used to calculate the convective fluxes. Venkatakrisnan's limiter is applied to the primitive variables. Turbulent variables for the SA model are convected using a first-order scalar upwind method. The gradients of the variables are computed using a weighted least-squares method. An adaptive CFL is used for convergence acceleration.

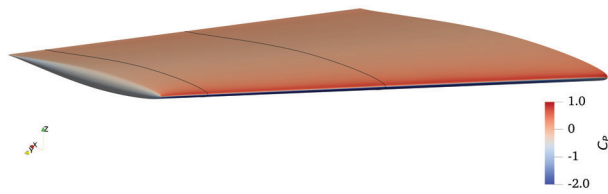
The flow field remains constant for both cases and is initially assessed. The flow field prediction is compared with the experimental measurements in Fig. 3 at two spanwise stations. The location of the two spanwise stations are shown in Fig. 3a. While the numerical predictions of the pressure coefficient distribution are compared to the experimental measurements in Figs. 3b & 3c. In general, the pressure coefficient distribution is in close agreement with the measurements on both the upper and lower surface of the wing and the leading edge suction peak is captured.

The numerical methods for computing the collection efficiency are now introduced. A forward Euler integration scheme is used to integrate the particle trajectories with an integration time step of 10^{-5} s. A cloud of 56 250 000 supercooled water droplets is initialised using a KD tree at approximately 3 spanwise lengths upstream of the wing. The cloud of supercooled water droplets is tracked in the computational domain for 0.1 s until all particles have impacted with the wing and the collection efficiency is computed.

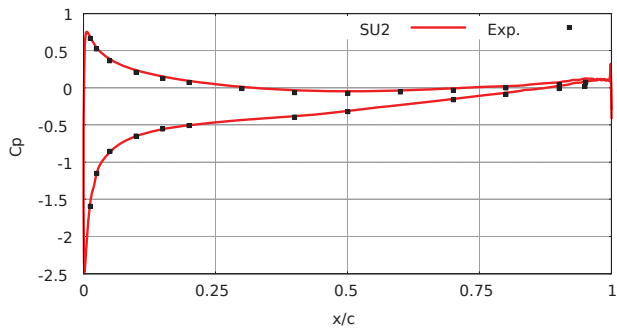
Case-111 is used to assess the water droplet impingement model in Appendix C operating conditions. The numerical predictions are compared with the experimental recordings in Fig. 4. Impingement data was again obtained at two spanwise stations as shown in Fig. 4a. The prediction of the collection efficiency on the swept horizontal tail is shown in Fig. 4b. Only the experimental data at the inboard station is displayed for clarity due to high similarity in the measurements. The collection efficiency peak and droplet impingement limits are well represented.

Case-112 is used to assess the water droplet impingement model in Appendix O operating conditions. These operating conditions require the introduction of a splashing model due to the presence of super-cooled large water droplets. The splashing model used in the submission to the 1st Ice Prediction Workshop for the code-to-code was based on a modified version of the Trujillo splashing model [27] as used by LEWICE-3D code [28, 29]. Numerical and experimental predictions are presented at the same spanwise stations as Case-111. The results are shown in Fig. 5. It can be observed that while the impingement limits and peak are relatively well captured, the prediction on the upper surface of the wing is not. The splashing model over predicts the mass of water which splashes on impact with the upper surface.

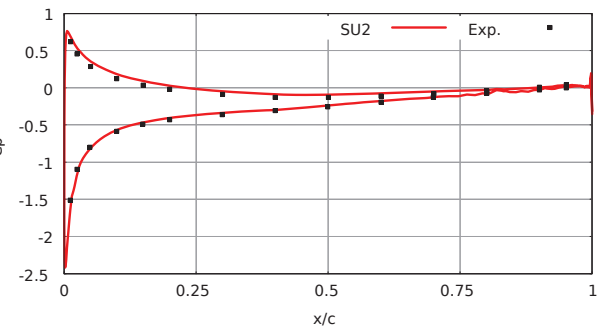
To further investigate, an assessment of different wall interaction modelling techniques is presented in Fig. 6. It is observed that the collection efficiency is significantly over predicted on the upper surface without modelling splashing effects. A simplified rebound model displays similar characteristics to using no splashing model at the peak. However, further aft where the impact angle is greater, the model predicts the rebound of particles leading to a sharp reduction in the collection efficiency. The LEWICE-3D splashing model [28, 29] is subsequently compared to the standard Trujillo splashing model [30]. The LEWICE-3D splashing model results are in good correlation with the experimental measurement at the peak, while standard Trujillo splashing model under predicts the peak collection efficiency. However both models over predict the mass of splashed water droplets slightly aft of the peak. The tail of the collection efficiency curve is well predicted by both splashing models.



(a) Surface pressure coefficient distribution with selected spanwise stations.



(b) Pressure coefficient distribution at the inboard location $y = 24$ in.



(c) Pressure coefficient distribution at the inboard location $y = 43$ in.

Fig. 3 NACA 64A008 swept tail pressure coefficient distribution at two inboard and outboard spanwise locations compared to experimental data from Ref.[26].

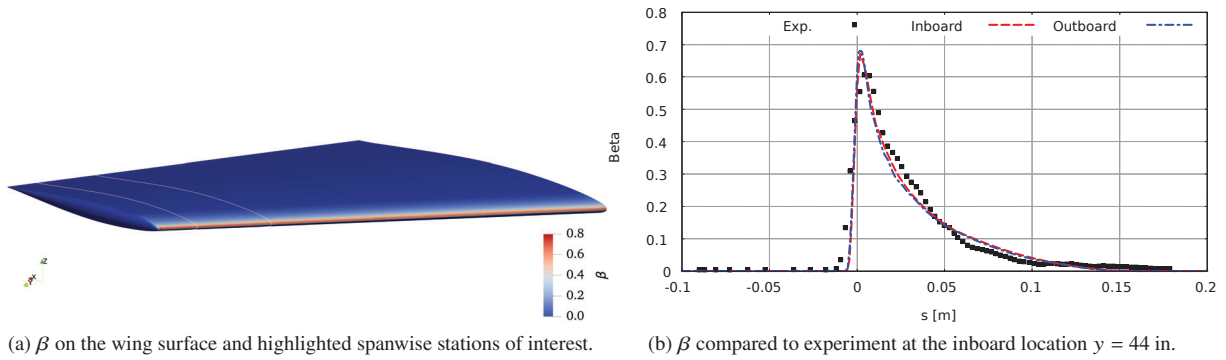


Fig. 4 NACA 64A008 swept tail collection efficiency, β , with a MVD = $21\mu\text{m}$ compared to experimental data from Ref.[26] at two inboard and outboard spanwise locations.

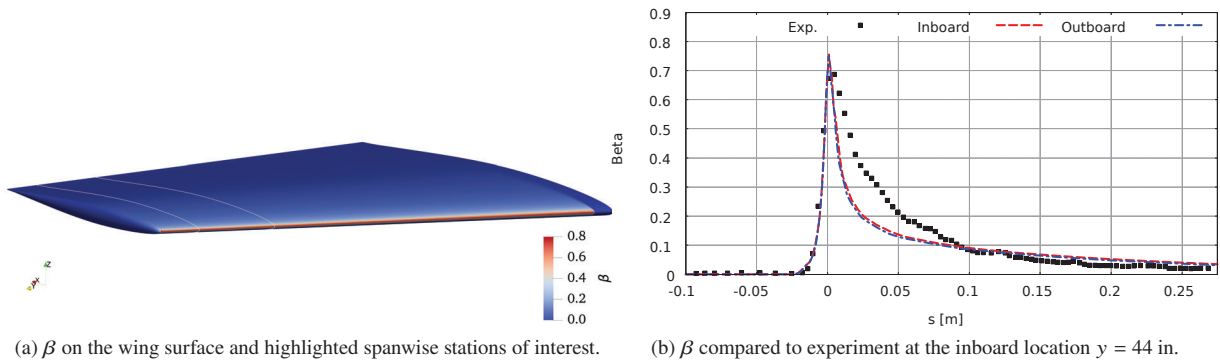


Fig. 5 NACA 64A008 swept tail collection efficiency, β , with a MVD = $92\mu\text{m}$ compared to experimental data from Ref.[26] at two inboard and outboard spanwise locations.

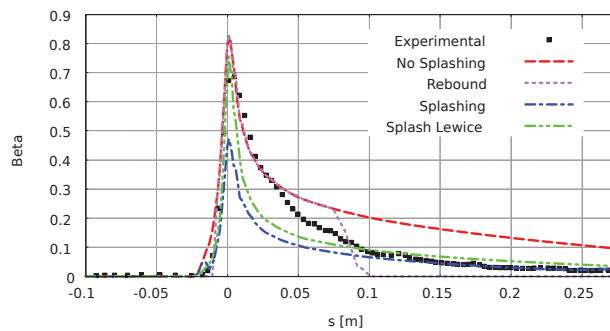


Fig. 6 Comparison of impingement models at the inboard spanwise location for Case-112.

B. Case-121, 122

The second test case presented are Case-121 and Case-122. The focus of these test cases is to assess the prediction of the collection efficiency on complex multi-component geometries. Likewise to the first set of test cases, the experimental database generated by Papadakis et al. [26] is used for the preliminary validation of models. The configuration of Case-121 and Case-122 is a three-element-airfoil. The three-element-airfoil was initially designed in the 1990's as an advanced high lift system which was representative of modern transport wing designs. The design was selected to address the needs of large transport air-framers. The operational test conditions of Case-121 are displayed in Table 3. The flow field validation was conducted at $AoA = 0^\circ$ meanwhile the droplet impingement validation was conducted at $AoA = 4^\circ$.

Table 3 Three-Element-Airfoil Test Conditions Ref. [26].

Mach	AoA	Pressure	Temp	MVD	Re	Chord
[-]	[$^\circ$]	[Pa]	[K]	[μm]	[-]	[in]
0.23	0.0, 4.0	84,337	291.2	21, 92	4.9×10^6	36

The flow field of the high lift three-element-airfoil is complex with strong regions of flow separation. As a consequence, a mesh sensitivity analysis was conducted. The first mesh used was provided from the 1st Ice Prediction Workshop and is referred to as G1. While the second mesh was generated using an in-house grid generation software called uhMesh [31] and is referred to as G2. The two mesh are displayed in Fig. 7. The baseline mesh is considered as G1 while the fine mesh is considered as G2. G1 contains approximately 54 000 volume elements meanwhile the slat, main, and flap airfoil elements are respectively Discretized by 130, 256, and 125 surface elements. G2 contains approximately 700 000 volume elements which are primarily located in the near-field region close to the airfoil. The slat, main, and flap airfoil elements are respectively composed of 588, 2262, and 941 surface elements. Both mesh use a structured boundary layer to ensure $y^+ < 1$ everywhere.

The numerical methods for computing the flow field in SU2 are now introduced. The convective fluxes for the flow equations are computed using the Jameson-Schmidt-Turkel's (JST) scheme. Venkatakrishnan's limiter is applied to the primitive variables. Turbulent variables for the SA model are convected using a first-order scalar upwind method. The gradients of the variables are computed using a weighted least-squares method. An adaptive CFL is used for convergence acceleration.

The sensitivity of the flow solution to the mesh resolution is displayed in Fig. 8. In general, the flow solutions from G1 and G1 are comparable and both mesh capture the essential flow characteristics of the high-lift three-element-airfoil. However on closer examination, in key regions of interest, slight differences are visible. The region in close proximity to the slat is displayed in Figs. 8c & 8d. Significant flow separation is displayed on the pressure side of the slat due to the high curvature. The strength of the vortical structure in G2 appears stronger and more defined. Moreover, this impacts the stagnation point of the main airfoil element. The second area of interest is the cove region of the main element and the flap and is displayed in Figs. 8e & 8f. The cove region towards the trailing edge of the main element exhibits strongly separated flow. This region of separated flow is noticeably greater in G2. In addition, the vortex produced by the sharp trailing edge of the slat is better preserved in G2 and its influence on the suction side of the flap is highlighted. Consequently, G2 is used for the remaining studies due to the particle trajectories being dependent on the flow solution.

The pressure coefficient from the numerical prediction is compared to the experimental measurements in Fig. 9. The numerical predictions compare favourably with the experimental measurements on the main and flap elements. The contrary is however true for the slat element with the numerical predictions and experimental measurements showing significant discrepancies which are thought to be an effect of the highly separated flow.

The flow characteristics of the high lift three-element-airfoil are complex and depend on the operating conditions. While the pressure coefficient measurements were conducted at $AoA = 0^\circ$, the collection efficiency measurements were conducted at $AoA = 4^\circ$. The influence of the AoA on the flow field is displayed in Fig. 10. At $AoA = 0^\circ$, the AoA relative to the slat is greater meaning there is a larger region of separated flow on the pressure side of the slat when compared to $AoA = 4^\circ$ as shown in Figs. 10a & 10b. Additionally, the stagnation point of each element depends on the AoA . There is also a strong region of recirculating flow in the cove region near the lower side of of the main element's trailing edge which is present at both AoA as shown in Figs. 10c & 10d. At $AoA = 0^\circ$ the region of recirculating flow extends slightly further downstream. The influence of the AoA on the flap element appears minimal.

The numerical settings for computing the collection efficiency are now addressed. A front of particles in injected

at a distance of 4 chord lengths in front of the airfoil. This value was chosen as the minimum distance presenting an unperturbed flow and it was selected by performing preliminary runs and checking the value of beta. The number of particles is automatically adapted by checking the L2 norm of two consecutive beta calculations. New particles are injected as long as the difference is greater than a user prescribed tolerance. In this case it was set to $3e - 3$, which amount to a total number of particles of 200 000. Particle diameter distribution was discretized by means of the experimental 27 bins distribution provided. Computationally, this accounts to performing 27 individual simulations and obtain the collection efficiency as a weighted sum of each contribution.

The collection efficiency results for Case-121 are shown in Fig. 11. The overall distribution of the collection efficiency curves are captured. However, on the slat airfoil element there is an offset in the prediction towards the lower surface as shown in Fig. 11a. Meanwhile the numerical results slightly under predict the collection efficiency on the lower surface of the main and flap elements as shown in Figs. 11b & 11c. Meanwhile the collection efficiency results for Case-122 are shown in Fig. 12. In general the trends are similar to Case-121 however the main element displays higher discrepancies with the experimental measurements which is thought to be attributed to droplet splashing effects.

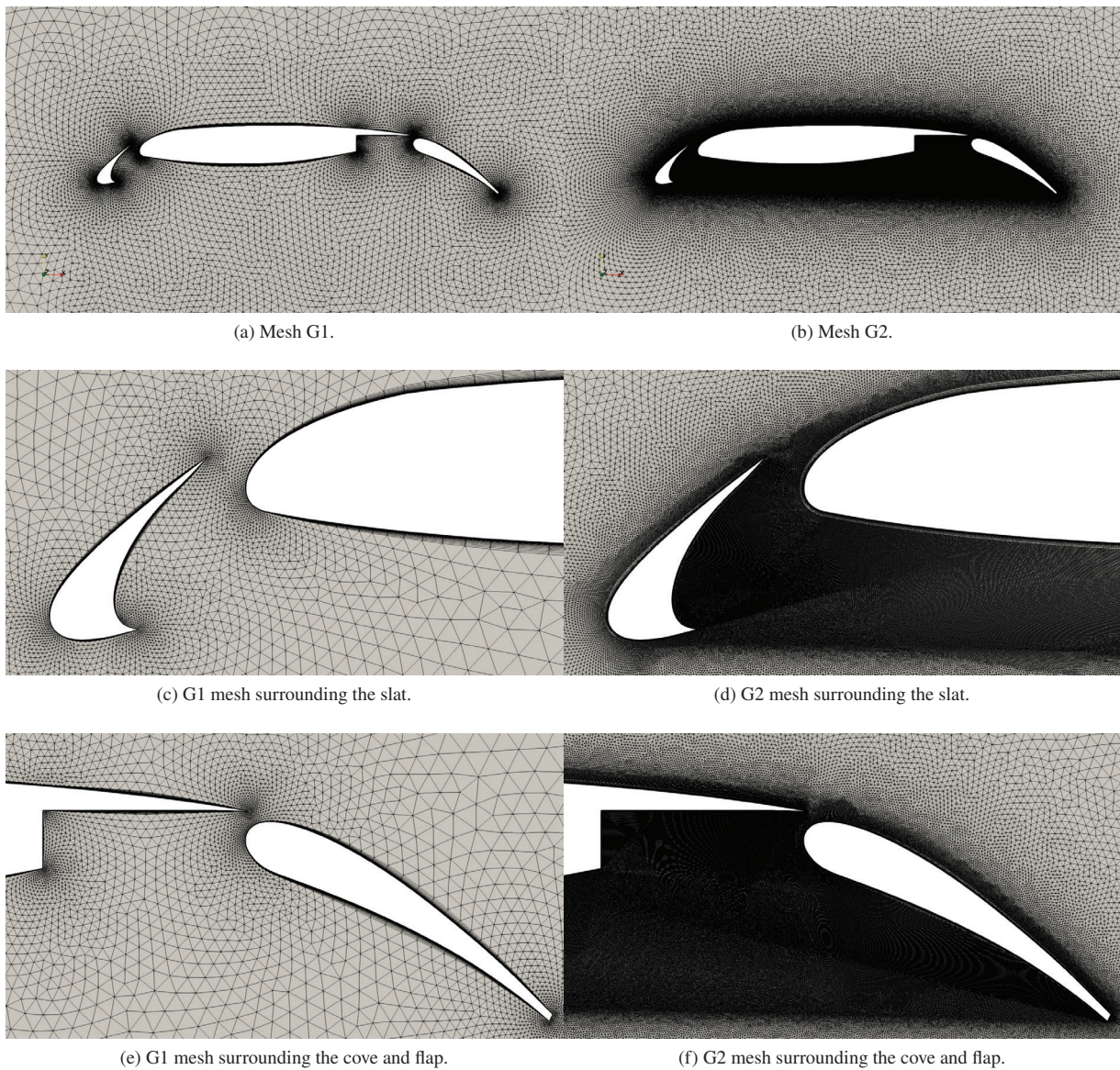


Fig. 7 Levels of mesh refinement for G1 and G2.

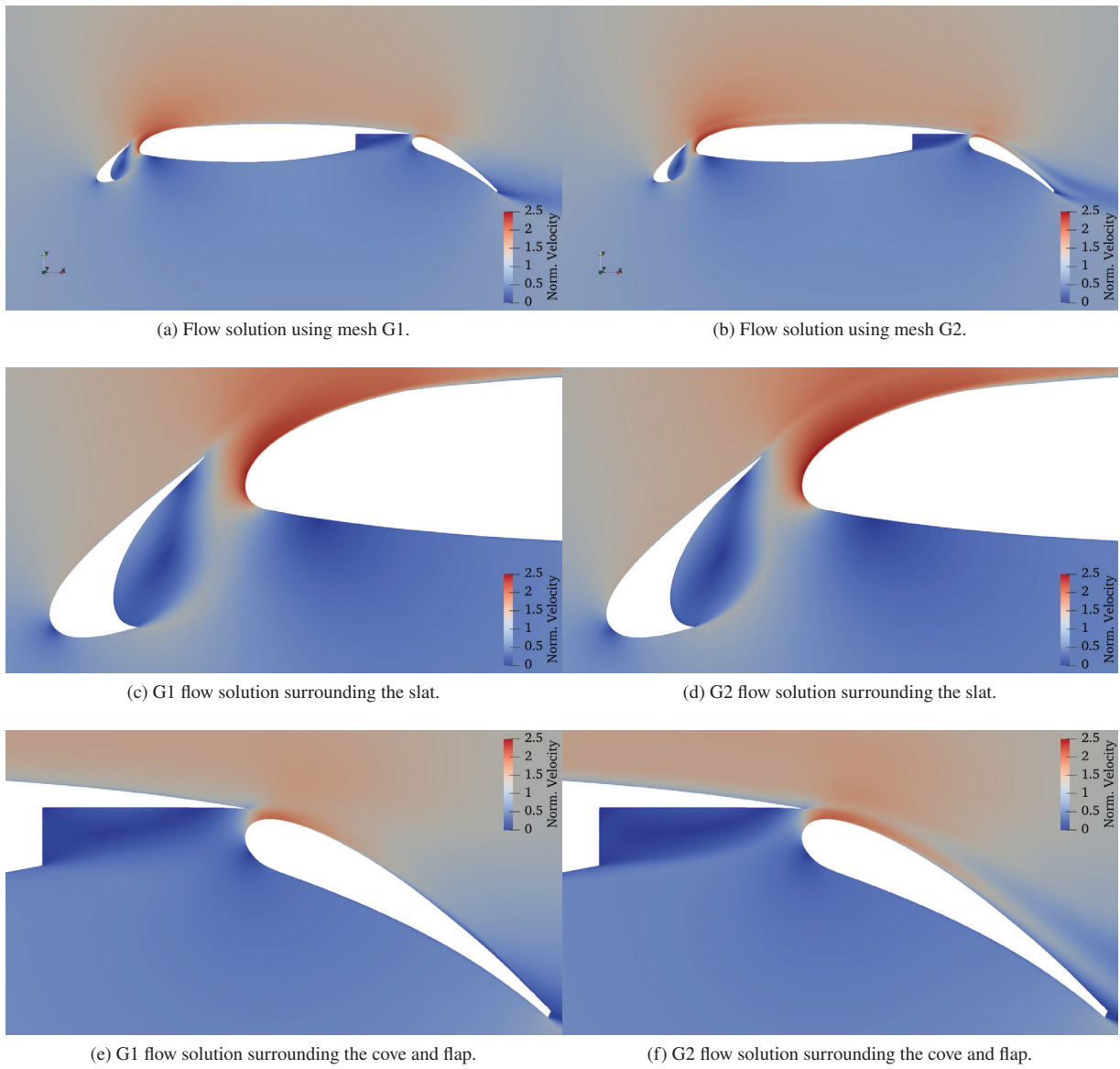


Fig. 8 Sensitivity of the flow solution to the mesh resolution. Displaying the normalized velocity magnitude.

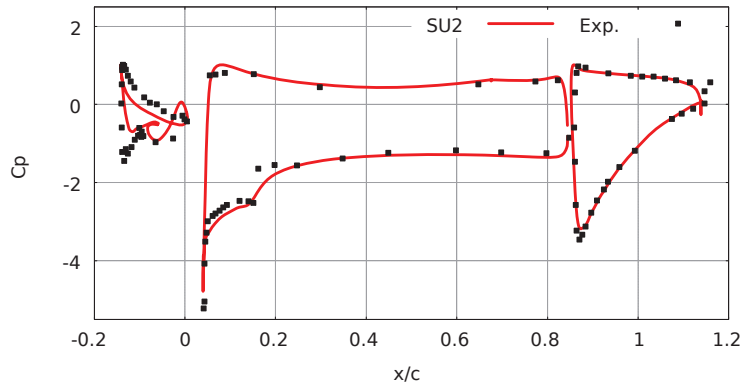


Fig. 9 Comparison of the pressure coefficient prediction on three-element-airfoil with experimental measurements from Ref. [26].

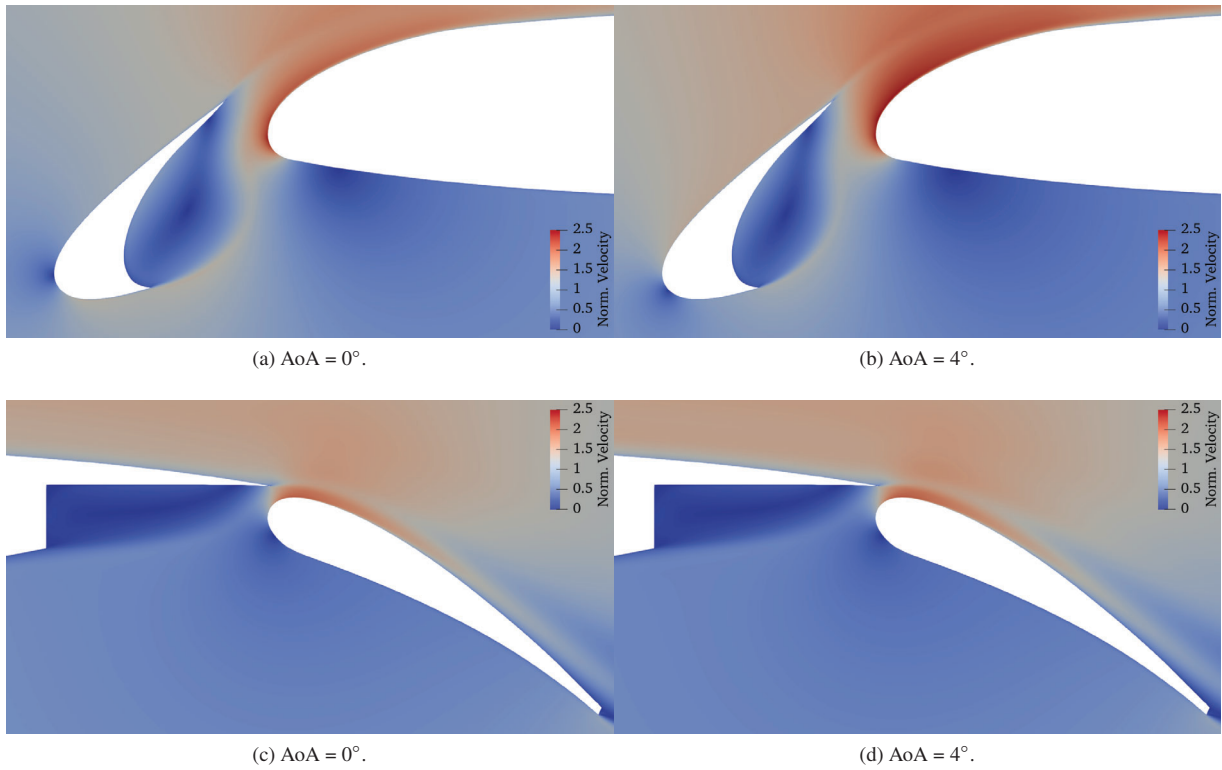
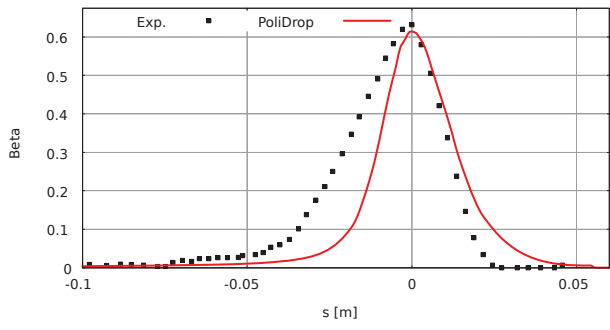
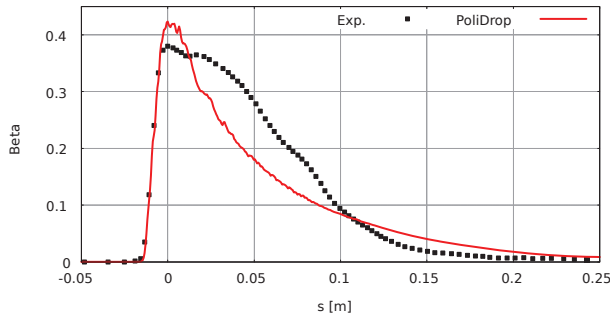


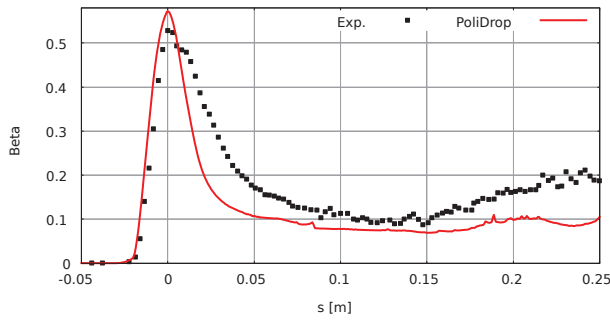
Fig. 10 Influence of the AoA on the leading edge region of the three-element-airfoil. Displaying the normalized velocity magnitude.



(a) Slat element.

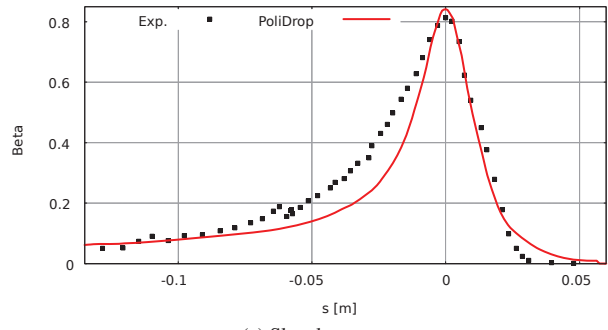


(b) Main element.

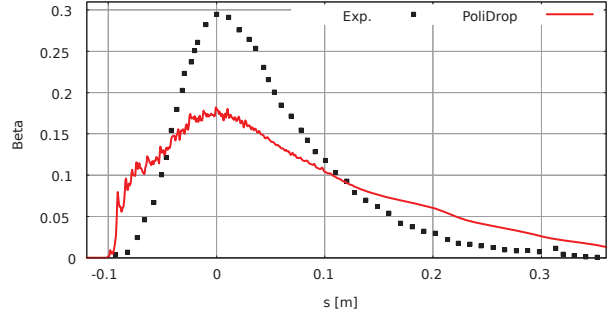


(c) Flap element.

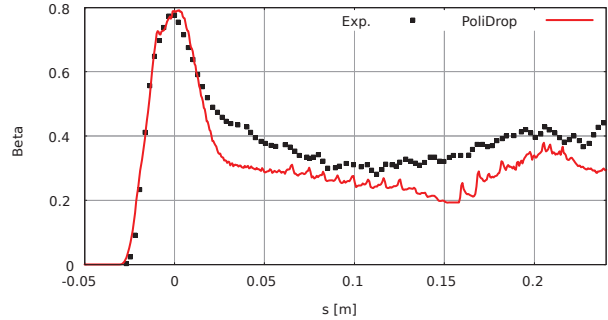
Fig. 11 Comparison of the collection efficiency predictions on Case-121 with experimental measurements taken from Ref. [26].



(a) Slat element.



(b) Main element.



(c) Flap element.

Fig. 12 Comparison of the collection efficiency predictions on Case-122 with experimental measurements taken from Ref. [26].

C. Case-241, 242

The third test cases presented are Case-241 and Case-242. The test cases were part of work to develop and validate a three-dimensional scanning system to record ice accretion geometry. The two-dimensional straight wing ice scans from Lee et al. [32] are used for the assessment of the numerical ice predictions. The conditions from Case-241 correspond to streamwise rime icing conditions, while the conditions from Case-242 correspond to glaze icing conditions which produce ice horns. The test conditions are displayed in Table 4.

Table 4 Horizontal Tail Test Conditions Ref. [32].

Mach	AoA	Temp	MVD	LWC	Re	Chord
[-]	[°]	[K]	[μm]	[g m^{-3}]	[-]	[in]
0.3	2.0	257, 266	15, 30	0.4, 0.75	3.5×10^6	18

A multi-step simulation is performed for case-241 and 242, creating a new body-fitted mesh at each time-step with an in-house grid generation software called uhMesh [31]. At each time-step, the solid boundary is retrieved through a Level-Set based novel approach [33] and with the open-source software Mmg [34]. To perform a mesh sensitivity analysis, different grid sizes have been tested. Each mesh is characterized by the ratio of the minimal leading edge size to the airfoil chord h_{min}/c . The medium and fine mesh for the case-241 are characterized by $h_{min}/c = 0.002$ and $h_{min}/c = 0.001$, leading to an initial mesh of approximately 63 000 and 70 000 elements respectively. The medium and fine mesh for the 242-case are characterized by $h_{min}/c = 0.001$ and $h_{min}/c = 0.0005$, leading to an initial mesh of approximately 70000 and 88000 elements respectively. Each mesh use a structured boundary layer to ensure $y^+ < 1$ everywhere.

The numerical methods for computing the flow field in SU2 are now discussed. Roe's second-order upwind scheme is used to calculate the convective fluxes. Venkatakrisnan's limiter is applied to the primitive variables. Turbulent variables for the SA model are convected using a first-order scalar upwind method. The gradients of the variables are computed using a weighted least-squares method. An adaptive CFL is used for convergence acceleration.

The numerical techniques and parameters for computing the collection efficiency are now introduced. A forward Euler integration scheme is used to integrate the particle trajectories with an integration time step of 10^{-5} s. A cloud of initially 120 supercooled water droplets is progressively refined until two successive values of the $L2$ norm of the collection efficiency β fall below the threshold of $3e-6$. The cloud is located at approximately 3 chord lengths upstream of the airfoil. The cloud of supercooled water droplets is tracked in the computational domain for 0.1 s until all particles have impacted with the airfoil and the collection efficiency is computed.

The models and parameters used to for the ice prediction are now addressed. Multi step ice accretion is performed for these test cases, subdividing the total exposure time in equally smaller time intervals. To perform a sensitivity analysis, different time intervals have been tested. The model used in these test cases to help capture the complex experimental ice shapes is the local exact solution of the unsteady Stefan problem for the temperature profiles within the ice layer in glaze conditions. The local surface temperature is used for the heat exchange. A steady liquid film model is used with an integration time step of 1 s. The rime and glaze ice density are respectively 880 kg m^{-3} and 917 kg m^{-3} .

The ice prediction results for the straight wing configuration are shown in Figs. 13 & 14. The two dimensional simulation results are compared to the Maximum Combined Cross Section (MCCS) of the experimental ice scans from Lee et al. [32]. The conditions from Case-241 are representative of the rime ice regime which the numerical prediction captures as shown in Fig. 13. The numerical prediction over predicts the ice thickness on the leading edge when compared to the MCCS. The conditions from Case-242 are representative of the glaze ice regime and consequently horn ice shapes are produced as shown in Fig. 14. The PoliMIce framework predicts complex two-dimensional ice shapes which exhibit strong similarities to the MCCS experimental measurements. Parameters which strongly influence the final ice shape are displayed in Figs. 15. It shows that the mesh sensitivity and number of multi-step time intervals have a greater influence on glaze ice shapes. Both the mesh refinement and number of multi-step time intervals impact the size and angle of the ice horns.

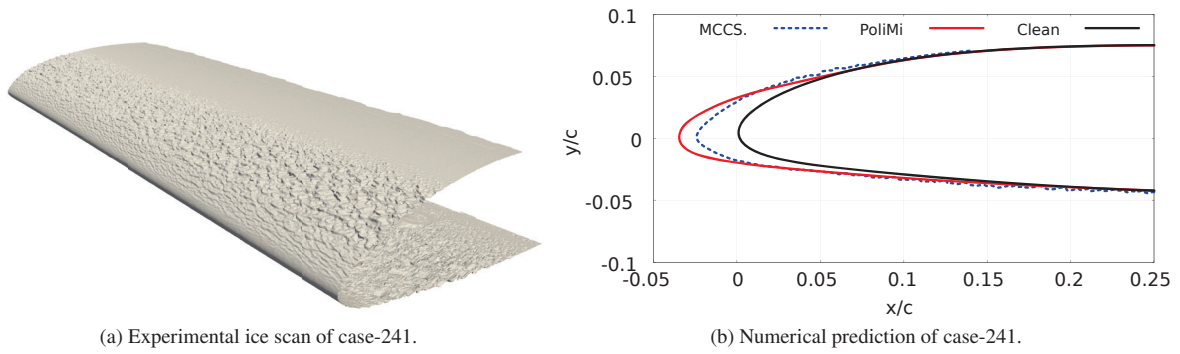


Fig. 13 Comparison of ice prediction with experimental ice measurements displaying the Maximum Combined Cross Section (MCCS). Experimental ice scans taken from Lee et al. [32].

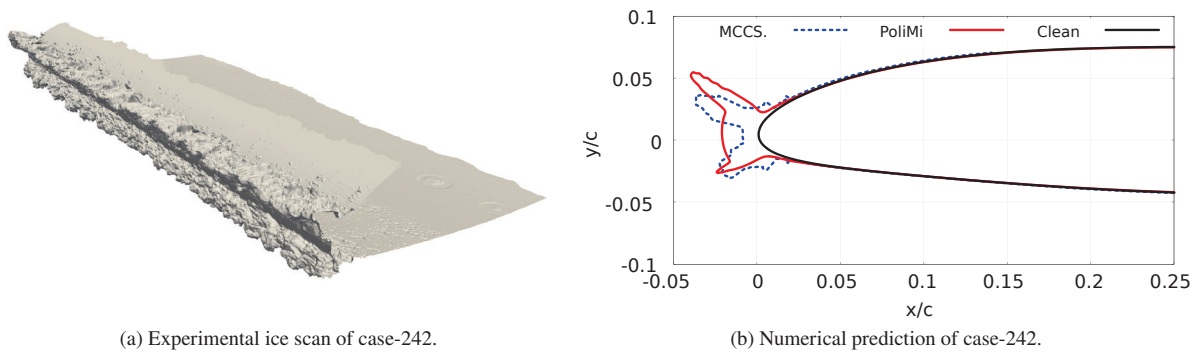


Fig. 14 Comparison of ice prediction with experimental ice measurements displaying the Maximum Combined Cross Section (MCCS). Experimental ice scans taken from Lee et al. [32].

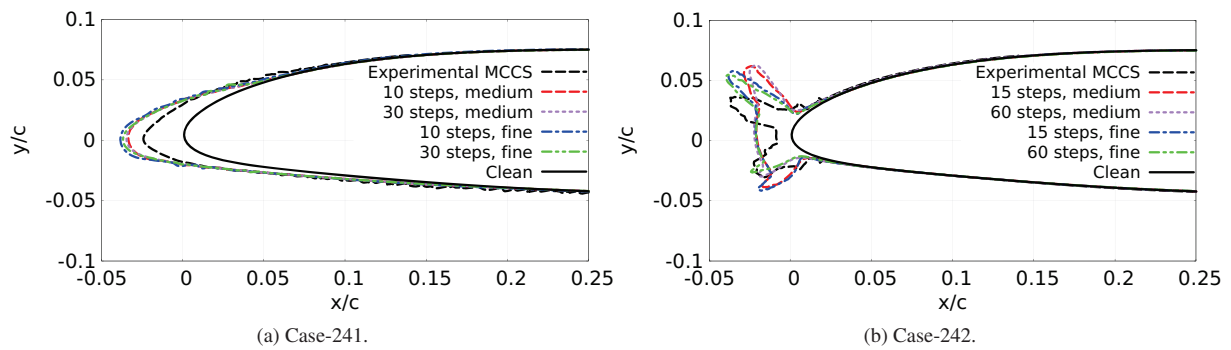


Fig. 15 Mesh and time step sensitivity analysis.

D. Case-361, 362, 371, 372

The final set of test cases simulated are Case-361, 362, 371, and 372. The experimental ice tracings measured by Bidwell [35] on a wing with 30° and 45° sweep angles in the NASA IRT are used for validation of the ice prediction models. In particular the experiments were setup to evaluate a void density model for predicting complex features of scallop ice shapes. The model wing has a symmetric NACA 0012 profile and the wing tunnel operating conditions are shown in Table 5. The swept wing geometry and spanwise location of ice tracings are displayed in Fig. 16.

Table 5 NACA 0012 Swept Wing Test Conditions Ref. [35].

Mach	AoA	Temp	Pressure	MVD	LWC	Re	Chord
[-]	[°]	[K]	[Pa]	[μm]	[g m^{-3}]	[-]	[in]
0.3	0.0	257, 266	92321, 94463	32	0.45, 0.47	7.2×10^6	36



Fig. 16 NACA 0012 Swept wing geometry at 30° and 45° sweep angles and spanwise stations where the ice tracings were measured.

The mesh provided by the 1st Ice Prediction Workshop are used for simulating Case-361, 362, 371, and 372. The mesh generated with the 30° sweep angle contains approximately 8 394 000 volume elements and approximately 102 000 surface elements are used for the discretization of the wing geometry. Meanwhile mesh generated with the 45° sweep angle contains approximately 8 018 000 volume elements and approximately 97 000 surface elements are used for the discretization of the wing geometry. Both mesh use a structured boundary layer which satisfies $y^+ < 1$ to fully resolve viscous effects within the boundary layer. The external NASA IRT walls are incorporated in the mesh. Inlet and outlet boundary conditions are subsequently applied to the appropriate wind tunnel boundaries.

The numerical methods for computing the flow field in SU2 are now discussed. Roe's second-order upwind scheme is used to calculate the convective fluxes. Venkatakrishnan's limiter is applied to the primitive variables. Turbulent variables for the SA model are convected using a first-order scalar upwind method. The gradients of the variables are computed using a weighted least-squares method. An adaptive CFL is used for convergence acceleration.

The numerical techniques and parameters for computing the collection efficiency are now addressed. A forward Euler integration scheme is used to integrate the particle trajectories with an integration time step of 10^{-5} s. A cloud of 9 000 000 supercooled water droplets is initialised using a KD tree at approximately 2.5 spanwise lengths upstream of the wing. The cloud of supercooled water droplets is tracked in the computational domain for 0.1 s until all particles have impacted with the wing and the collection efficiency is computed.

The models and parameters used to for the ice prediction are hereinafter introduced. Single step ice accretion is performed for these three-dimensional test cases. The model used in these test cases to help capture the complex experimental ice shapes is the local exact solution of the unsteady Stefan problem for the temperature profiles within the ice layer in glaze conditions. The local surface temperature is used for the heat exchange. A steady liquid film model is

used with an integration time step of 1 s. The rime and glaze ice density are respectively 880 kg m^{-3} and 917 kg m^{-3} .

The ice prediction results for the wing with the 30° sweep angle namely Case-361 and Case-362 are shown in Figs. 17 & 18. The three-dimensional ice shapes are displayed in Fig. 17 and the comparison with the experimental measurements is shown in Fig. 18. The lower temperature condition produces a *spearhead* ice shape characteristic of the rime ice regime. The general shape of the rime ice is captured although the roughness is not. The higher temperature condition produces a more challenging *double-horn* glaze ice structure. The angle of the horns is relatively well predicted although there is an under prediction in the overall mass of ice accreted.

The ice prediction results for the wing with the 45° sweep angle namely Case-371 and Case-372 are shown in Figs. 19 & 20. Similar trends to the wing with the 30° sweep angle are observed. However increasing the sweep angle increases the three-dimensional effects and as a result there are larger discrepancies in the results.

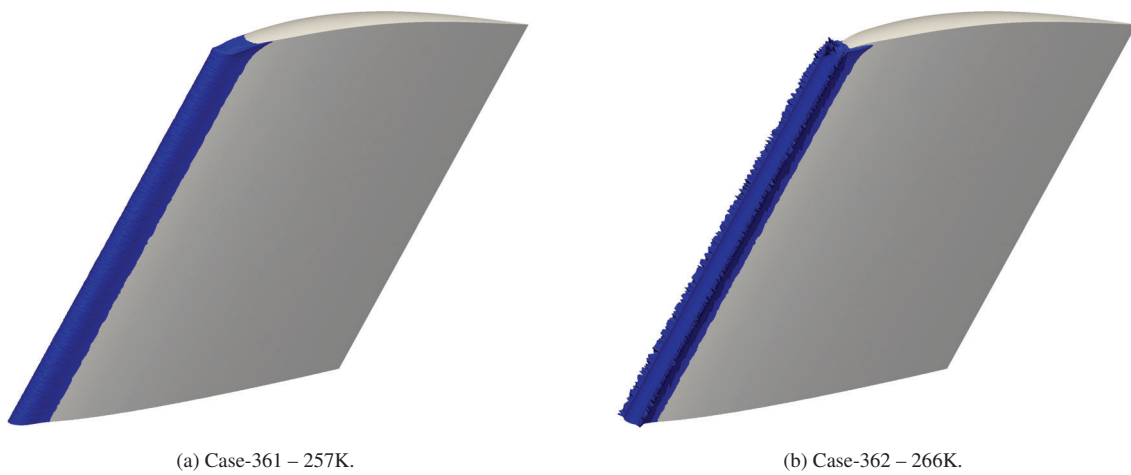


Fig. 17 Three-dimensional ice shape predictions on the 30° swept wing during the rime and glaze ice regime.

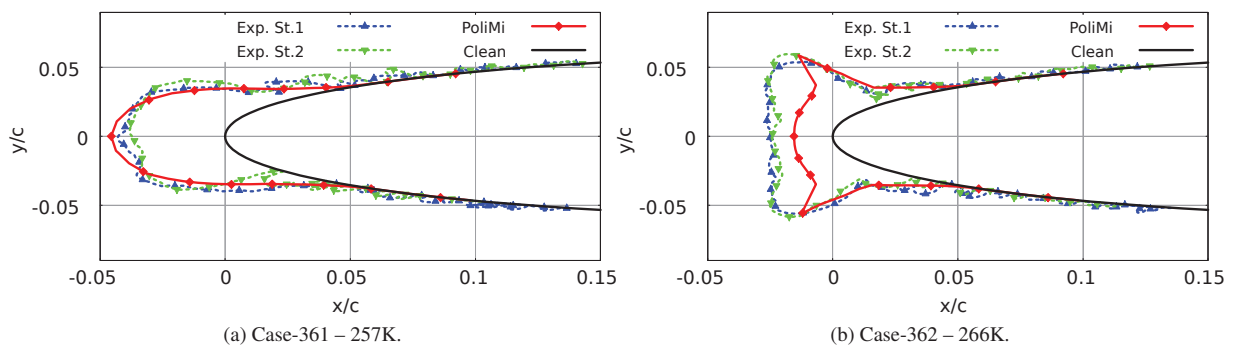


Fig. 18 Ice shape comparison with experimental measurements on the 30° swept wing from Ref. [35] during both the rime and glaze ice regime.

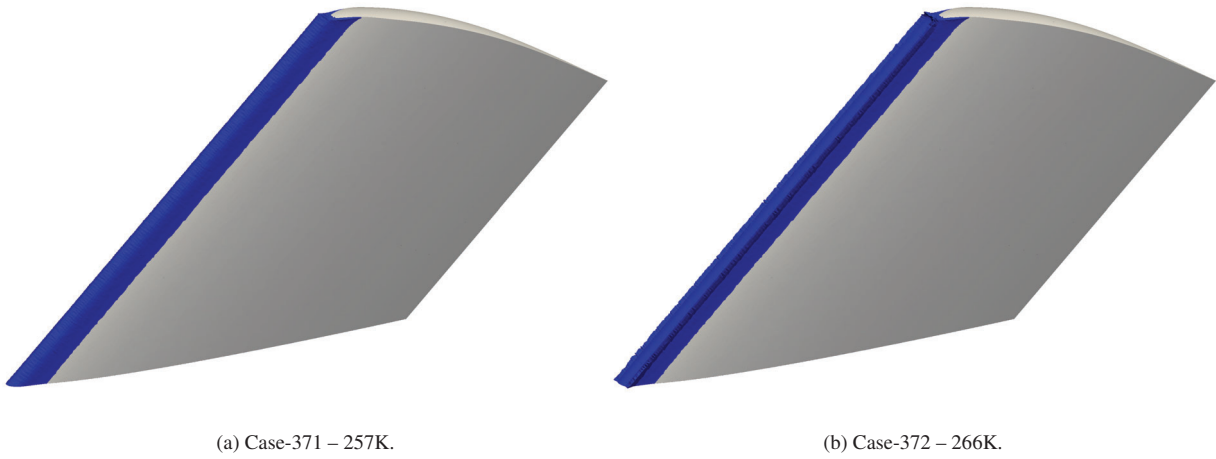


Fig. 19 Three-dimensional ice shape predictions on the 45° swept wing during the rime and glaze ice regime.

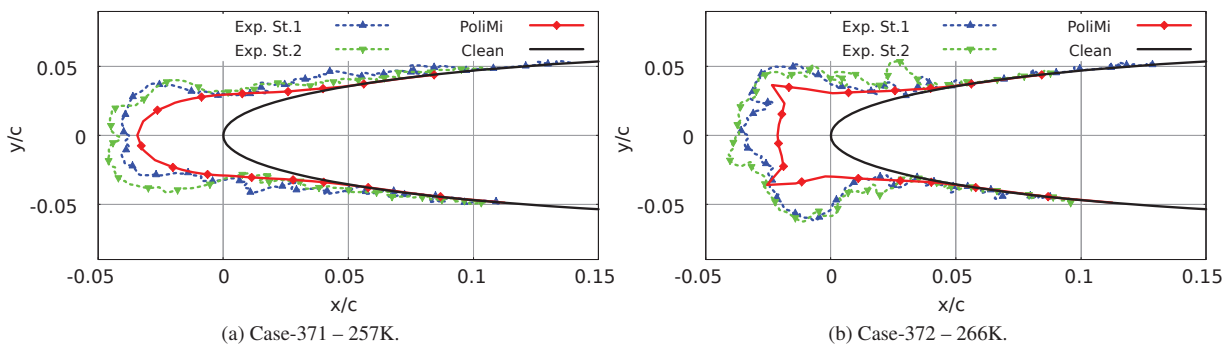


Fig. 20 Ice shape comparison with experimental measurements on the 45° swept wing from Ref. [35] during both the rime and glaze ice regime.

V. Conclusion

In this paper, Politecnico di Milano Icing Research Group's results from the 1st AIAA Ice Prediction Workshop are presented. A series of two- and three-dimensional test cases are simulated to assess the PoliMIce Framework. In general, the collection efficiency and ice accretion results are in good agreement with the experimental data. In particular this includes the collection efficiency results in Appendix C operating conditions and the ice prediction during the rime regime. However, there remains scope for improvement as highlighted by the more challenging configurations and test conditions. The high-lift three-element-airfoil configuration was a demanding test case for droplet impingement due to the presence of shadow regions. Additionally discrepancies between collection efficiency numerical predictions and experimental measurements exist during Appendix O operating conditions even with state-of-the-art splashing models. Furthermore, all of the glaze ice regime test conditions remain a challenge for current ice prediction models. Finally, techniques to improve the robustness of three-dimensional multi-step ice accretion simulations are a requirement for the progression of numerical ice prediction codes. Current developments focus on re-meshing or adaptation strategies to conform the body fitted mesh to the moving boundaries (see e.g. [36]) in the framework of multi-step ice accretion.

Acknowledgments

The ICE GENESIS project has received funding from the European Union's Horizon 2020 research and innovation program under grant agreement no. 824310.

References

- [1] Gent, R., Dart, N., and Cansdale, J., "Aircraft Icing," *Philosophical Transactions of the Royal Society of London. Series A: Mathematical, Physical and Engineering Sciences*, Vol. 358, No. 1776, 2000, pp. 2873–2911. <https://doi.org/10.1098/rsta.2000.0689>.
- [2] Huet, F., and Moller, M., "ICE GENESIS Overview," Presented at the International Conference on Icing of Aircraft, Engines, and Structures (SAE 2019), June 2019.
- [3] Broeren, A., et al., "1st Ice Prediction Workshop," Workshop run in conjunction with the AIAA AVIATION FORUM 2021, 26-29 June 2021. Virtual Event.
- [4] Wright, W. B., "User's Manual for LEWICE Version 3.2," Tech. Rep. NAS3-00145, National Aeronautics and Space Administration, Glenn Research Center, Cleveland, Ohio 44135, 1 November 2008.
- [5] Beaugendre, H., Morency, F., and Habashi, W. G., "FENSAP-ICE's three-dimensional in-flight ice accretion module: ICE3D," *Journal of aircraft*, Vol. 40, No. 2, 2003, pp. 239–247.
- [6] Gori, G., and Zocca, M., and Garabelli, M., and Guardone, A., and Quaranta, G., "PoliMIce: A Simulation Framework for Three-Dimensional Ice Accretion," *Applied Mathematics and Computation*, Vol. 267, 2015, pp. 96–107. DOI: 10.1016/j.amc.2015.05.081.
- [7] Gori, G., and Parma, G., and Zocca, M., and Guardone, A., "Local Solution to the Unsteady Stefan Problem for In-Flight Ice Accretion Modeling," *Journal of Aircraft*, Vol. 55, No. 1, 2017, pp. 251–262. DOI: <https://doi.org/10.2514/1.C034412>.
- [8] Morelli, M., "Simulation and Detection of Ice Formation and Shedding on Rotorcraft," Ph.D. thesis, Politecnico di Milano, February 2021.
- [9] Morelli, M., and Guardone, A., "A simulation framework for rotorcraft ice accretion and shedding," *Aerospace Science and Technology*, 2021, p. 107157. <https://doi.org/https://doi.org/10.1016/j.ast.2021.107157>.
- [10] Morelli, M., Zhou, B. Y., and Guardone, A., "Acoustic Characterization of Glaze and Rime Ice Structures on an Oscillating Airfoil via Fully Unsteady Simulations," *Journal of the American Helicopter Society*, Vol. 65, No. 4, 2020, pp. 1–12.
- [11] Zhou, B. Y., Gauger, N. R., Hauth, J., Huan, X., Morelli, M., and Guardone, A., "Towards Real-Time In-Flight Ice Detection Systems via Computational Aeroacoustics and Machine Learning," *Aerodynamic Design/Shape Optimization Session at the AIAA Aviation*, Dallas, Texas, 17-21 June, 2019, p. 3103.
- [12] Arizmendi, B., Noce, A. D., Gallia, M., Bellosta, T., and Guardone, A., "Numerical simulation of a thermal Ice Protection System including state-of-the-art liquid film model," *Journal of Computational and Applied Mathematics*, Vol. 391, 2021, p. 113454. <https://doi.org/https://doi.org/10.1016/j.cam.2021.113454>, URL <https://www.sciencedirect.com/science/article/pii/S037704272100073X>.
- [13] Arizmendi, B., "Robust Optimization of a Thermal Ice Protection System in Uncertain Cloud Environments," Ph.D. thesis, Politecnico di Milano, February 2021.
- [14] Arizmendi, B., Gallia, M., Gori, G., Congedo, P., and Guardone, A., "Robust Bi-Objective Optimization of the Heat Flux Distribution for an Airfoil Thermal Anti-Ice Protection System in Uncertain Operational Clouds," *Atmospheric and Space Environments Session at the AIAA AVIATION Forum*, Virtual Event, 2-6 August, 2021.
- [15] Gori, G., Congedo, P. M., Le Maître, O., Bellosta, T., and Guardone, A., "Modeling In-Flight Ice Accretion Under Uncertain Conditions," *Journal of Aircraft*, 2021, pp. 1–15. <https://doi.org/10.2514/1.c036545>.
- [16] Economon, T. D., and Palacios, F., and Copeland, S. R., and Lukaczyk, T. W., and Alonso, J. J., "SU2: An Open-Source Suite for Multiphysics Simulation and Design," *AIAA Journal*, Vol. 54, No. 3, 2015, pp. 828–846. DOI: <https://doi.org/10.2514/1.J053813>.
- [17] Morelli, M., Bellosta, T., and Guardone, A., "Development and preliminary assessment of the open-source CFD toolkit SU2 for rotorcraft flows," *Journal of Computational and Applied Mathematics*, Vol. 389, 2021, p. 113340.
- [18] Re, B., and Abgrall, R., "Non-equilibrium Model for Weakly Compressible Multi-component Flows: The Hyperbolic Operator," *Lecture Notes in Mechanical Engineering*, Springer International Publishing, 2020, pp. 33–45. https://doi.org/10.1007/978-3-030-49626-5_3.
- [19] Bellosta, T., Parma, G., and Guardone, A., "A Robust 3D Particle Tracking Solver for In-Fight Ice Accretion Using Arbitrary Precision Arithmetic," *VIII International Conference on Computational Methods for Coupled Problems in Science and Engineering*, 2019.

- [20] Morelli, M., Bellosta, T., and Guardone, A., “Lagrangian Particle Tracking in Sliding Mesh Applicable for Rotorcraft Icing Applications,” *45th European Rotorcraft Forum*, Warsaw, Poland, 7–20 September, 2019, pp. 1–13.
- [21] Stefan, J., “Ueber die Theorie der Eisbildung, insbesondere über die Eisbildung im Polarmeere,” *Annalen der Physik*, Vol. 278, No. 2, 1891, pp. 269–286. <https://doi.org/https://doi.org/10.1002/andp.18912780206>, URL <https://onlinelibrary.wiley.com/doi/abs/10.1002/andp.18912780206>.
- [22] Gori, G., Parma, G., Zocca, M., and Guardone, A., “Local Solution to the Unsteady Stefan Problem for In-Flight Ice Accretion Modeling,” *Journal of Aircraft*, Vol. 55, No. 1, 2018, pp. 251–262. <https://doi.org/10.2514/1.C034412>.
- [23] Morelli, M., Bellosta, T., and Guardone, A., “Efficient radial basis function mesh deformation methods for aircraft icing,” *Journal of Computational and Applied Mathematics*, Vol. 392, 2021, p. 113492.
- [24] Wang, G., Mian, H. H., Ye, Z.-Y., and Lee, J.-D., “Improved Point Selection Method for Hybrid-Unstructured Mesh Deformation Using Radial Basis Functions,” *AIAA Journal*, Vol. 53, No. 4, 2015, pp. 1016–1025. <https://doi.org/10.2514/1.J053304>.
- [25] Xie, L., and Liu, H., “Efficient Mesh Motion Using Radial Basis Functions With Volume Grid Points Reduction Algorithm,” *Journal of Computational Physics*, Vol. 348, 2017, pp. 401–415. <https://doi.org/10.1016/j.jcp.2017.07.042>.
- [26] Papadakis, M., Hung, K. E., Vu, G. T., Yeong, H. W., Bidwell, C. S., Breer, M. D., and Bencic, T. J., “Experimental Investigation of Water Droplet Impingement on Airfoils, Finite Wings, and an S-Duct Engine Inlet,” National Aeronautics and Space Administration, Glenn Research Center, Technical Memorandum No. 2002-211700, October 2002.
- [27] Dezitter, F., “ONICE2D and DROP3D SLD capability assessment,” In: *SAE 2011 International Conference on Aircraft and Engine Icing and Ground Deicing*, SAE Technical Paper 2011-38-0088, Warrendale, PA, 2011. <https://doi.org/doi:10.4271/2011-38-0088>.
- [28] Wright, W., “Validation results for LEWICE 3.0,” *43rd AIAA Aerospace Sciences Meeting and Exhibit*, Reno, Nevada, anuary 10–13, 2005, p. 1243.
- [29] Wright, W., “Further refinement of the LEWICE SLD model,” *44th AIAA Aerospace Sciences Meeting and Exhibit*, Reno, Nevada, January 9–12, 2006, p. 464.
- [30] Trujillo, M., Mathews, W., Lee, C., and Peters, J., “Modelling and experiment of impingement and atomization of a liquid spray on a wall,” *International Journal of Engine Research*, Vol. 1, No. 1, 2000, pp. 87–105.
- [31] Dussin, D., Fossati, M., Guardone, A., and Vigevano, L., “Hybrid grid generation for two-dimensional high-Reynolds flows,” *Computers & fluids*, Vol. 38, No. 10, 2009, pp. 1863–1875.
- [32] Lee, S., Broeren, A. P., Kreeger, R. E., Potapczuk, M. G., and Utt, L., “Implementation and validation of 3-D ice accretion measurement methodology,” *6th AIAA Atmospheric and Space Environments Conference*, Atlanta, GA, USA, 16–20 June, 2014, p. 2613. <https://doi.org/10.2514/6.2014-2613>.
- [33] Donizetti, A., Re, B., and Guardone, A., “A level-set based mesh adaptation technique for mass conservative ice accretion in unsteady simulations,” *9th International Conference on Computational Methods for Coupled Problems in Science and Engineering, COUPLED PROBLEMS 2021*, CIMNE, 2021, pp. 1–11. <https://doi.org/10.23967/coupled.2021.004>.
- [34] Dapogny, C., Dobrzynski, C., and Frey, P., “Three-dimensional adaptive domain remeshing, implicit domain meshing, and applications to free and moving boundary problems,” *Journal of Computational Physics*, Vol. 262, 2014, pp. 358–378.
- [35] Bidwell, C. S., “Icing Analysis of a Swept NACA 0012 Wing Using LEWICE3D Version 3.48,” *6th AIAA Atmospheric and Space Environments Conference*, Atlanta, GA, USA, 16–20 June, 2014. URL <https://arc.aiaa.org/doi/abs/10.2514/6.2014-2200>, <https://doi.org/10.2514/6.2014-2200>.
- [36] Cirrotola, L., Ricchiuto, M., Froehly, A., Re, B., Guardone, A., and Quaranta, G., “Adaptive deformation of 3D unstructured meshes with curved body fitted boundaries with application to unsteady compressible flows,” *Journal of Computational Physics*, Vol. 433, 2021, p. 110177. <https://doi.org/https://doi.org/10.1016/j.jcp.2021.110177>.